ACS APPLIED MATERIALS & INTERFACES

Research Article

www.acsami.org

Engineering the Morphology and Configuration of Ternary Heterostructures for Improving Their Photocatalytic Activity

Kui Li, Rong Chen, Shun-Li Li, Shuai-Lei Xie, Xue-Li Cao, Long-Zhang Dong, Jian-Chun Bao,* and Ya-Qian Lan*

Jiangsu Key Laboratory of Biofunctional Materials, School of Chemistry and Materials Science, Nanjing Normal University, Nanjing, 210023 Jiangsu, P. R. China

Supporting Information

ABSTRACT: Heteronanomaterials composed of suitable semiconductors enable the direct conversion from solar power into clean and renewable energy. Ternary heterostructures with appropriate configuration and morphology possess rich and varied properties, especially for improving the photocatalytic activity and stability synchronously. However, suitable ternary heterostructure prototypes and facile while effective strategy for modulating their morphology and configuration are still scarce. Herein, various ternary ZnS-CdS-$Zn_{1-x}Cd_xS$ heterostructures with tunable morphology (0 to 2 D) and semiconductor configurations (randomly distributed, interface mediated, and quantum dots sensitized core@shell heterostructures) were facilely synthesized via one-pot hydrothermal method resulting from the different molecular structures of the amine solvents. Semiconductor morphology, especially configuration of the ternary heterostructure, shows dramatic effect on their photocatalytic activity. The CdS sensitized porous $Zn_{1-x}Cd_xS$@ZnS core@shell takes full advantage of ZnS, $Zn_{1-x}Cd_xS$ and CdS and shows the maximal photocatalytic H_2-production rate of 100.2 mmol/h/g and excellent stability over 30 h. This study provides some guidelines for the design and synthesis of high-performance ternary heterostructure via modulation of semiconductor configuration and morphology using one-pot method.

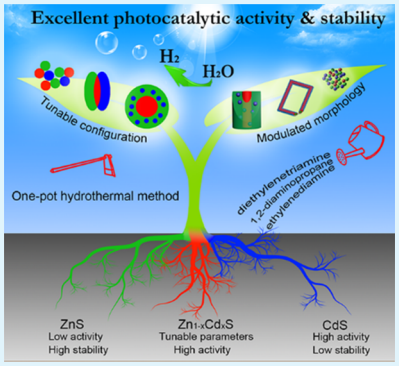

KEYWORDS: *ternary heterostructure, morphology, configuration, photocatalytic activity, core−shell*

1. INTRODUCTION

Semiconductor heteronanomaterial with appropriate configuration and morphology enables the direct conversion from solar power into clean and renewable hydrogen energy via photocatalytic water splitting.[1−7] However, most of the heterostructures are based on two semiconductors,[8−10] the binary heterostructure, which may suffer from the drawbacks including poor band structure matching and large lattice stress due to the distinct intrinsic parameters of the two semiconductors.[11,12] The noble metal cocatalysts (such as Pt, Pd, Au) were adopted to further facilitate the separation and transport of photogenerated charge carriers.[13,14] Embedding a cost-effective semiconductor with suitable parameter and feature into the traditional binary heterostructure could improve the separation and transport efficiency of charge carriers,[2] thus increasing the photocatalytic activity and stability simultaneously. Additionally, rational design of ternary heterostructure could bring out rich and varied properties via modulating the configuration.[2,15,16] To the best of our knowledge, suitable ternary heterostructure prototypes are still scarce, and the modulation of their configuration and morphology with facile method is still a grand challenge.

To date, most of the semiconductor heterostructures are fabricated at least by two steps using surface modification process, that is, one semiconductor is fabricated on the surface of another one, which largely restricts the scale-up synthesis of heterostructure photocatalysts[17] and decreases the number of active sites. One-pot method, which involves the reconstruction of the precursors and bulk fabrication of heterostructure could facilitate the thoroughgoing reaction of the reactants and increases the heterostructure active sites. Moreover, the modulation of the morphology and semiconductor configuration of the heterostructures could increase the number of exposed active sites[5,18−24] and enhance the separation and transport efficiency of charge carriers, respectively. Nevertheless, both the fabrication of heterostructures, especially the ternary heterostructures, and the modulation of their morphology and configuration using one-pot method are rarely reported.

ZnS with a wide bandgap possesses negligible visible light photocatalytic activity and excellent stability,[8,17] whereas CdS shows excellent photocatalytic activity but very poor lifetime.[25,26] $Zn_{1-x}Cd_xS$, the "alloy" of ZnS and CdS, possesses continuously tunable bandgap (E_g) ranging from 3.66 (ZnS) to 2.4 eV (CdS) and lattice constant between 0.331 (⟨100⟩ of ZnS) and 0.359 nm (⟨100⟩ of CdS).[3,27−29] Also, $Zn_{1-x}Cd_xS$ exhibits a better photocatalytic activity than that of single CdS, even loaded with Pt as cocatalyst.[29] Constructing the ternary

Received: November 24, 2015
Accepted: February 2, 2016
Published: February 2, 2016

DOI: 10.1021/acsami.5b11388
ACS Appl. Mater. Interfaces 2016, 8, 4516−4522

heterostructure of ZnS-CdS-$Zn_{1-x}Cd_xS$ with suitable configuration via a facile one-pot method could not only relieve the structure mismatch,[30] but also improve the photocatalytic stability due to the different characteristics of ZnS, CdS, and $Zn_{1-x}Cd_xS$. In this regard, rational design of the morphology and configuration of the ternary ZnS-CdS-$Zn_{1-x}Cd_xS$ heterostructure via a simple method for completely utilizing the features of these semiconductors is of special importance from both the scientific and practical viewpoints. Although all these semiconductors and the heterostructures between ZnS and CdS have been extensively investigated as photocatalysts,[8,17,25,26,31] the $Zn_{1-x}Cd_xS$ based heterostructures, especially the ZnS-CdS-$Zn_{1-x}Cd_xS$ ternary heterostructure as photocatalysts, have been researched scarcely.

Herein, ZnS, CdS, and $Zn_{1-x}Cd_xS$ were adopted for constructing the ternary heterostructures to take advantage of the different merits of these semiconductors. Both the morphology (0D to 2D) and semiconductor configurations (randomly distributed, interface mediated, and quantum dots sensitized core@shell heterostructures) were facilely modulated via a one-pot hydrothermal method using different solvents (ethylenediamine, EDA; 1,2-diaminopropane, DAP; diethylenetriamine, DETA; deionized water, DIW) with different molecular structures as templates. The photocatalytic activity was found to be dominated by the morphology, especially the semiconductor configuration. The rational designed CdS sensitized porous $Zn_{1-x}Cd_xS$@ZnS core@shell heterostructure completely utilizes the features of the semiconductors[4,22,32] and shows the maximal photocatalytic rate of 100.2 mmol/h/g (apparent quantum efficiency = 38.4%) and excellent stability. This value is 143- and 911-times higher than that of CdS prepared with DETA and DIW as solvents, respectively.

2. EXPERIMENTAL SECTION

2.1. Sample Preparation. In a typical synthesis of the ZnS-DETA hybrid nanomaterial precursor, 1.5 mmol of $ZnCl_2$ and 3.0 mmol of CN_2H_4S (thiourea) were dissolved in 30 mL of pure DETA under ultrasound until all the reagents were dissolved. This solution was subsequently transferred into 50 mL Teflon-lined autoclave and maintained at 180 °C for 21 h. The final white products were rinsed and dried at 60 °C overnight. Thirty milligrams of the as-prepared ZnS-DETA precursor was dissolved in 10 mL of DIW under ultrasound for a few minutes. Given contents of $Cd(NO_3)_2{\cdot}4H_2O$ with different Cd/(Zn+Cd) molar ratios (0, 10, 30, and 50 at%) were dissolved in DIW (2.8 mL) and then dropped into the aforementioned solution quickly under mild stirring. After several minutes, the obtained solution was transferred into 15 mL autoclave and maintained at 140 °C for different times (2, 3, 4, 6, 8, 10, 15, 20, 24, and 30 h). The final products were rinsed and dried at 60 °C overnight in the vacuum oven to evaporate the solvent. The heterostructures (the Cd content of 30 at%, reaction time of 10 h) derived from EDA, DAP, and DIW were fabricated with the same parameters using different solvents as templates.

2.2. Characterization. X-ray diffraction (XRD) patterns were recorded on a D/max 2500 VL/PC diffractometer (Japan) equipped with graphite monochromatized Cu Kα radiation (λ = 1.54060 Å). The transmission electron microscopy (TEM) and high-resolution TEM (HRTEM) images were recorded on JEOL-2100F apparatus at an accelerating voltage of 200 kV. The morphology was investigated by a field emission scanning electron microscope (SEM, JSM-7600F) at an acceleration voltage of 10 kV. The energy-dispersive X-ray spectroscopy (EDX) was conducted on JSM-5160LV-Vantage typed energy spectrometer. UV−visible diffused reflectance spectra were recorded using a Cary 5000 UV−vis spectrometer (Viarian, USA) with $BaSO_4$ as a reflectance standard. The Brunauer−Emmett−Teller (BET) specific surface area (S_{BET}), nitrogen adsorption, and water vapor adsorption of the heterojunction samples were analyzed by an Autosorb-iQ adsorption apparatus (Quantachrome instruments, USA). The BET surface area was determined by a multipoint BET method using adsorption data in the relative pressure (P/P_0) range of 0.05−0.3. A desorption isotherm was used to identify the pore size distribution via the Barret−Joyner−Halender (BJH) method by assuming a cylindrical pore model. Electrochemical impedance spectra (EIS) measurements were carried out via an electrochemical workstation (EC-lab, SP-150, VMP3-based instruments, America) under a surface power density of about 0.1 mW/cm^2 using Na_2S (0.1 M) and Na_2SO_3 (0.02 M) mixture solution as the supporting electrolyte. The photoluminescence (PL) spectra were performed on a Molecular Fluorescence Spectrometer (Cary Eclipse, Varian Associates, America). The PEC measurements were performed with a Zahner PEC workstation (Zahner, Germany). All experiments were carried out at room temperature using a conventional three-electrode system with a modified ITO electrode (sheet resistance 20−25 Ω/square) with a geometrical area of 0.25 cm^2 as the working electrode, a platinum wire as the auxiliary electrode, and a Ag/AgCl electrode as the reference electrode. All of the PEC measurements were carried out under 430 nm of irradiation at a constant potential of 0.2 V in 0.1 M Na_2S + 0.02 M Na_2SO_3 mixed solutions under a surface power density of about 10 mW/cm^2. Element content analysis was tested on an Inductively Coupled Plasma (ICP) Spectroscope (Prodigy, Leeman, America). XPS data were collected using an X-ray photoelectron spectrometer (XPS) by a scanning X-ray microprobe (PHI 5000 Verasa, ULAC-PHI, Inc.) with Al Kα radiation and the C 1s peak at 284.6 eV as internal standard.

2.3. Photocatalytic Hydrogen Production. The photocatalytic H_2-production experiments were performed via a photocatalytic H_2-production activity evaluation system (CEL-SPH2N, CEAULight, China) in a 300 mL Pyrex flask, and the openings of the flask were sealed with silicone rubber septum. A 300 W xenon arc lamp through a UV-cutoff filter with a wavelength range of 420−1000 nm. The focused intensity on the flask was about 200 mW cm^{-2}. In a typical photocatalytic H_2-production experiment, 5 mg of the prepared photocatalyst was suspended in mixed solution containing Na_2S (0.35 M) and Na_2SO_3 (0.25 M). Before irradiation, the system was vacuumed for 5 min via the vacuum pump to completely remove the dissolved oxygen and ensure the reactor was in an anaerobic condition. The evolved H_2 content was analyzed by gas chromatography. Twenty milligrams of catalyst was used to measure the apparent quantum efficiency under the similar photocatalytic reaction conditions to the above-mentioned system using a filter at 420 nm (420 ± 8 nm).

3. RESULTS AND DISCUSSION

Various solvents (DAP, EDA, DETA, and DIW) were adopted to fabricate the ZnS precursors. Both the morphology and configuration of the ternary heterostructures (Cd/(Zn+Cd) = 30 at%) were modulated via a one-pot hydrothermal process for 10 h, and the corresponding samples were abbreviated as ZC-DAP, ZC-EDA, ZC-DETA, and ZC-DIW, respectively. All the heteronanomaterials show obvious ZnS, CdS, and $Zn_{1-x}Cd_xS$ phases and similar bandgap corresponding to CdS phase (Figures S1 and S2). Figure 1, panels a−c exhibit the TEM images of the distinct morphology of the ternary heterostructures derived from the different molecular structures of the amines (as shown in the inset). The morphology of these samples was further confirmed by SEM (Figure S3). In contrast to the nanoparticle morphology with a radius of about 2 μm of ZCS-DIW, the morphology of the heteronanomaterials could be modulated by the distinct molecular structures of the amines owing to the formation of ZnS-amines inorganic−organic hybrid templates.[3,9,33] The ZnS-EDA was sculpted layer by layer, and nanoframe morphology formed.[30] The side chain in DAP facilitates the formation of heterostructure with small nanoparticle morphology. Notably, the heteronanomaterial

DOI: 10.1021/acsami.5b11388
ACS Appl. Mater. Interfaces 2016, 8, 4516−4522

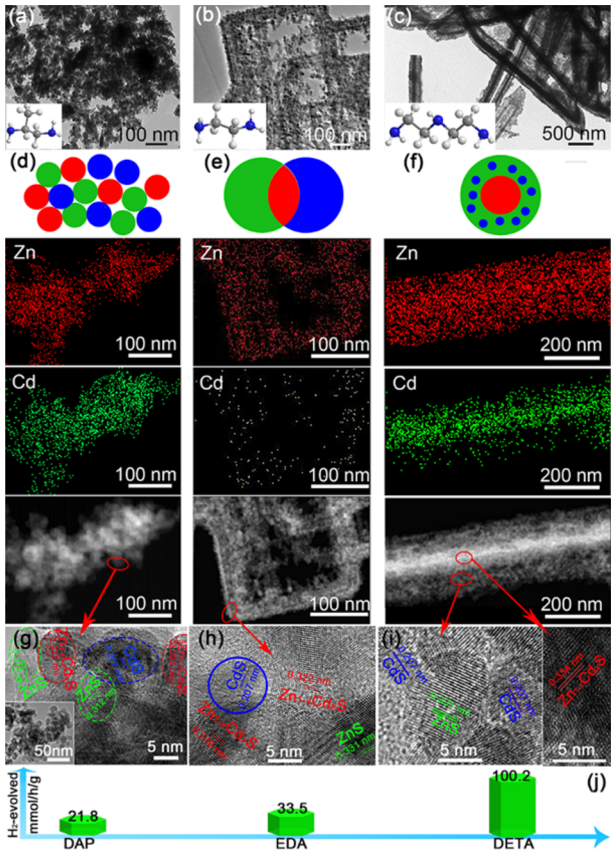

Figure 1. (a) Microstructure morphologies of (a) ZC-DAP, (b) ZC-EDA, and (c) ZC-DETA; insets demonstrate the ball and stick model of the amines. Schematic illustration of semiconductor configurations (green, ZnS; blue, CdS; red, $Zn_{1-x}Cd_xS$) and the element mapping of (d) ZC-DAP, (e) ZC-EDA, and (f) ZC-DETA. HRTEM images of (g) ZC-DAP (inset shows its TEM image), (h) ZC-EDA, and (i) ZC-DETA. (j) Dependence of photocatalytic H_2-production activity on the semiconductor morphology and configuration.

derived from DETA shows the core@porous shell structure with nanorod morphology.

The proposed semiconductor configurations (randomly distributed, interface mediated, and quantum dots sensitized core@shell heterostructures) and the element mapping of the ternary heteronanomaterials derived from DAP, EDA, and DETA were exhibited in Figure 1, panels d and f. ZC-DAP shows the randomly distributed heterostructure among ZnS, CdS, and $Zn_{1-x}Cd_xS$, as confirmed by the uniformly distributed of Zn and Cd in the whole skeleton of the connected nanoparticles from the element mapping, whereas the element mapping of ZC-EDA indicates that Cd is mainly distributed in the edge of the nanoframe, and the Cd content in the edge of the nanoframe (Figure S4) is higher than that in center of the nanoframe, which confirms the semiconductor configuration of $ZnS/Zn_{1-x}Cd_xS/CdS$ as reported in our previous work.[30] Fascinatingly, ZC-DETA exhibits CdS sensitized porous $Zn_{1-x}Cd_xS$@ZnS core@shell heterostructure. Both results of the element mapping and line scanning (Figure S5) indicate that Zn distributed in the matrix of the core−shell heterostructure uniformly, while Cd is mainly concentrated in the core region.

Semiconductor configurations of these ternary heterostructure were further confirmed by the HRTEM (Figure 1g−i). As exhibited from Figure 1, panel g, only one phase could be observed in single nanoparticle (inset of Figure 1g), and the ternary heterostructure in ZC-DAP is composed of the random distribution of the nanoparticles with different phases. As reported in our previous investigation,[30] the lattice fringe of $Zn_{1-x}Cd_xS$ could be observed between ZnS and CdS phases, indicating its configuration of $ZnS/Zn_{1-x}Cd_xS/CdS$. As depicted in Figure 1, panel i, CdS quantum dots (CdS QDs) with a diameter of approximately 5 nm are embedded in the highly porous ZnS shell, while only the $Zn_{1-x}Cd_xS$ lattice fringe is observed in core region. Moreover, all the heteronanomaterials derived from organic amines show higher N_2-adsorption volume and S_{BET} (Figure S6) than that of ZC-DIW. Characterizations for the composition of the samples derived from different amines via XPS and ICP (Figure S7) demonstrate that all the samples derived from different amines showed close Cd content, whereas ZC-DIW shows the much smaller Cd content (Figure S8) due to the incomplete reaction resulting from the larger particle size of ZnS (Figure S9).

Scheme 1 illustrates the evolution of morphology and configuration of the ternary heterostructures derived from

Scheme 1. Scheme Illustrating the Evolution of the Distinct Morphology and Configuration in the Heteronanomaterials Derived from (a) DETA, (b) EDA, and (c) DAP

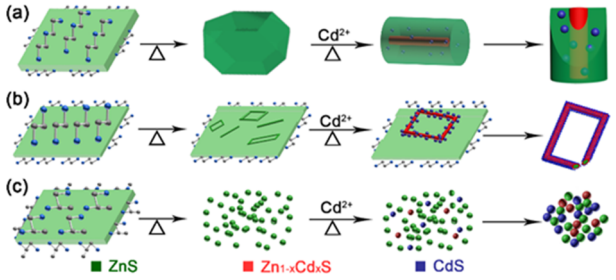

different templates with increased reaction time. ZnS derived from ZnS-DETA hybrid nanomaterials shows the porous morphology after the rapid dissolution of DETA molecules. This preformed porous ZnS, acting as shell and Zn and S sources, reacted with Cd^{2+} and generated the $Zn_{1-x}Cd_xS$ solid solution with nanorod morphology owing to the nanorod morphology of the CdS derived from amine,[34] which was surrounded by the remnant porous ZnS shell. Continuous reaction of ZnS and Cd^{2+} decreased the thickness of ZnS shell in longer reaction time, and the in situ formed CdS phase distributed in the matrix of ZnS porous shell through the cation exchange reaction between Cd^{2+} and ZnS.[35,36] Significantly, the larger radius of Cd^{2+} than that of Zn^{2+} is another reason for the formation of CdS phase.[27,37] ZnS derived from different amines with different reaction times, and the corresponding heterostructures were fabricated for systematically investigating the evolution mechanism of morphology. As shown in Figure S10, ZnS derived from EDA gradually dissolved with increased reaction time,[30] while ZnS-DAP and ZnS-DETA dissolved rapidly, and the nanoparticle and porous morphology were formed, respectively. Consequently, the corresponding ZnS-CdS-$Zn_{1-x}Cd_xS$ heterostructures derived from DETA, EDA, and DAP exhibited quantum dots sensitized core@shell nanorod, interface mediated nanoframe, and randomly distributed nanoparticle heterostructure, respectively.

The photocatalytic H_2-production via water splitting was chosen for evaluating the effect of morphology and configuration on the photocatalytic performance (Figure

DOI: 10.1021/acsami.5b11388
ACS Appl. Mater. Interfaces 2016, 8, 4516−4522

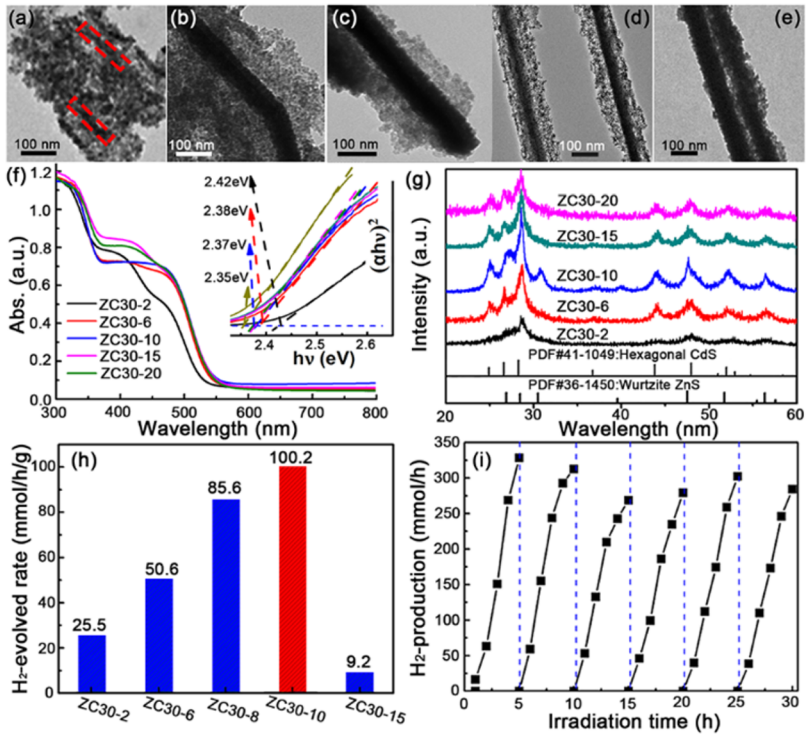

Figure 2. TEM images of ZC30 samples with processing times of (a) 2, (b) 6, (c) 8, (d) 10, and (e) 15 h, respectively. (f) UV−vis diffuse reflection spectra and the corresponding $(\alpha h\nu)^2$ versus $h\nu$ curves (inset), (g) XRD patterns, and (h) the comparison of the photocatalytic activity of the samples with different amount of Cd. (i) The photocatalytic stability of ZC30-10 without renewing the sacrificial solution.

1j).[3,27] Notably, the semiconductor morphology, especially configuration of the ternary heterostructure, showed distinct effect on their photocatalytic activity. All the heterostructures derived from amines possess much larger H_2-production activity than that of ZC-DIW (3.1 mmol/h/g) (Figure S11) because of their modulated morphology and more active sites as confirmed by the EDX results.[38] The $Zn_{1-x}Cd_xS$ interface-mediated heterostructure derived from EDA shows a better photocatalytic activity of 33.5 mmol/h/g than that of ZC-DAP (21.8 mmol/h/g) with randomly distributed heterostructure configuration. ZC-DETA exhibits the maximal H_2-evolution rate of 100.2 mmol/h/g because the CdS QDs sensitized $Zn_{1-x}Cd_xS$@porous ZnS core@shell heterostructure completely utilizes the features of ZnS, CdS, and $Zn_{1-x}Cd_xS$, and the porous ZnS shell facilitates the transport of reactants.[17] These results were further confirmed by the EIS spectra and transient photocurrent responses in Figure S12.

The formation mechanism of the CdS QDs sensitized $Zn_{1-x}Cd_xS$@ZnS core@shell heterostructure derived from DETA, and its effect on the photocatalytic activity was systematically investigated. A series of samples with nominal Cd/(Zn+Cd) molar ratio m were prepared and labeled as ZCm (m = 0, 10, 30, 50 at%). The XRD patterns and UV−vis diffuse reflection spectra (Figures S13 and S14) indicate that ZC10 possesses porous morphology with small irregular $Zn_{1-x}Cd_xS$ nanoregion owing to the rapid and complete reaction between the small amount of Cd and sufficient ZnS; ZC50 shows nanorod morphology with very flimsy porous shell due to the large Cd content. Notably, ZC30 with appropriate amount of Cd possesses nanorod core and considerable amount of porous shell (Figure S15). A composition variation is observed in ZC10 and ZC30 due to the complex ternary heterostructure (Figure S16). Moreover, ZC30 possesses considerable large S_{BET} of 81.5 m^2/g and the maximum water vapor adsorption volume (Figure S17). Consequently, ZC30 possesses the maximum H_2-production rate (Figure S18) because of its $Zn_{1-x}Cd_xS$@porous ZnS core−shell structure and large amount of CdS sensitized highly porous ZnS shell. The separation and transport efficiency were further confirmed by EIS spectra as shown in Figure S19.

To modulate the thickness of porous shell in the core−shell heterostructure derived from DETA, a series of samples (ZC30) with different reaction times were prepared and labeled as ZC30-n (n = 2, 4, 6, 8, 10, 12, 15, and 20 h). Figure 2, panels a−e demonstrate the TEM images of ZC30 with different reaction times. First, Cd^{2+} reacted with the sufficient ZnS for a short time of 2 h, forming an irregular $Zn_{1-x}Cd_xS$ nanoregion, which would become nanorod morphology in ZC30-6. The thickness of porous shell reduces with the increased reaction time, and ZC30-10 possesses a shell thickness of about 45 nm. However, the sample with longer reaction time (ZC30-15) shows very limited thickness of porous shell. Corresponding to the evolution of morphology, the content of Cd first increases with the reaction time increasing to 8 h owing to the decreased ZnS shell, while then it does not change dramatically in longer reaction time (Figure S20).

Effect of reaction time on the band structure of the heterostructure samples with 30 at% Cd was investigated by the UV−vis diffuse reflection spectra (Figure 2f). All the samples with different reaction times show two band edges in the UV and visible region, respectively. The E_g values corresponding to the absorption in visible region were calculated by the Kubelka−Munk (KM) method and demonstrated in the inset of Figure 2, panel f,[27] and no dramatic variation of band structure for CdS phase can be

DOI: 10.1021/acsami.5b11388
ACS Appl. Mater. Interfaces 2016, 8, 4516−4522

observed in the heterostructure samples prepared with different reaction times. However, the E_g corresponding to the absorption in the UV region keeps a constant value first and then decreases strongly owing to the disappearance of ZnS (Figure S21). The Zn content of the solid solution core of ZC30-10 was specified to be 48.5 at% (Figure S22).

Dependence of shell thickness on the photocatalytic H_2-evolution rate in the samples is exhibited in Figure 2, panel h. ZC30-10 shows the maximum value of 100.2 mmol/h/g and excellent apparent quantum efficiency (AQE) of 38.4% owing to the considerable amount of CdS and suitable thickness of shell.[39] This H_2-production rate is 143- and 911-times higher than that of CdS prepared using DETA and DIW as the solvents, respectively (Figure S23). In addition, the result is better than that of the previously reported CdS-based photocatalysts.[8,17,25,26,34,40−42] It is noteworthy that the photocatalytic H_2-production rate shows a sharp decline from 100.2 mmol/h/g in ZC30-10 to 9.2 mmol/h/g in ZC30-15, indicating the extremely momentous role of CdS sensitized porous ZnS shell in improving the photocatalytic H_2-production activity. Moreover, ZC30-10 shows excellent photocatalytic stability over a period of 30 h (Figure 2i), which is much better than that of $Zn_{1-x}Cd_xS$ interface mediated heterostructure (less than 20 h) because of the protective role of ZnS shell.[30] No obvious morphology variation is seen after the photocatalytic reaction of 30 h (Figure S24), which confirms that the CdS QDs sensitization could improve the photocatalytic activity of the shell without deteriorating its stability.[43] Interfacial electron transfer of the samples with different heterostructure configurations is investigated by EIS spectra (Figure S25). All the heterostructure samples show a much smaller semicircle in the middle-frequency region than that of CdS. Significantly, the smallest semicircle in the middle-frequency region in ZC30-10 indicates its highest efficiency of interfacial electron transfer stemming from its considerable amount of CdS/ZnS active sites.[9] Moreover, the core@shell heterostructure can be also obtained in ZC10 and ZC50 with reaction time of 24 and 3 h, respectively (Figure S26). However, the CdS phase is very weak, and the H_2-productin rate is lower than that of ZC30-10 (Figure S27). These results further confirm the growth manchansim of the core−shell morphology and the important role of CdS sensitized core@shell on the photocatalytic activity.

The transport and separation among ZnS, CdS, and $Zn_{1-x}Cd_xS$ are very important to evaluate the effect of semiconductor configuration on the photocatalytic activity. It was reported that the ZnS/CdS heterostructure exhibits the quasi-type II characteristics because of the acceptor states (I_s, V_{Zn}) in ZnS.[17,31,44,45] The defect states related acceptor levels in ZnS and $Zn_{1-x}Cd_xS$ were characterized by the PL spectra (Figure S28). All the heterostructure samples and the solid solution samples prepared via thermolysis method[27] with different amounts of Cd show the similar emission peak position derived from different defect states (such as V_{Zn}) to that in ZnS. These results were consistent with the previous publications,[46−48] which reported that the peak position of the emission derived from the defect states (such as V_{Zn}) in $Zn_{1-x}Cd_xS$ is similar to that in ZnS and will not change with the variation of E_g values derived from the different amounts of Cu^{2+} dopant. Consequently, the semiconductor with lower CB edge possesses lower defect (such as I_s and V_{Zn}) related acceptor level.

The excellent photocatalytic H_2-production in CdS QDs sensitized porous $Zn_{1-x}Cd_xS$@ZnS core−shell heterostructure under visible light irradiation can be exhibited by the schematic illustrations in Scheme 2. The photogenerated holes transferred

Scheme 2. Schematic Illustration for the Charge Transfer and Separation under Visible Light Irradiation in the Shell and Region near the Core of the Core−Shell Heterostructure, and the Proposed Mechanism for Photocatalytic H_2-Production under Visible Light Irradiation

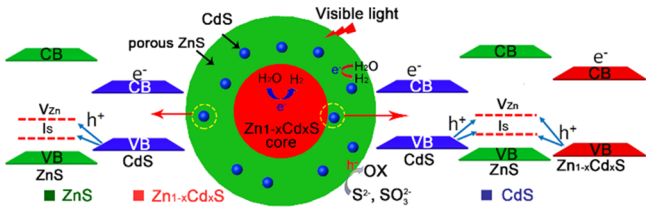

from the CdS to the acceptor states (V_{Zn} and I_S defect states) in porous ZnS shell.[17,31] On the other hand, the charge transport and separation among three components ($Zn_{1-x}Cd_xS$-ZnS-CdS) near the core is demonstrated in the left side of Scheme 2. The photogenerated holes were transferred from CdS and $Zn_{1-x}Cd_xS$ to the local acceptor states in ZnS shell due to the lower acceptor states in $Zn_{1-x}Cd_xS$ than that in ZnS.[46] In this regard, this core−shell heterostructure solves the two major obstacles of core@shell heterostructure: (i) poor photocatalytic activity of the single component in the core−shell heterostructure, especially the wide-bandgap protective shell,[17,49] and (ii) inferior lattice and band structure matching between the two semiconductors of the core−shell heterostructure.[11,12] Compared with the randomly distributed and $Zn_{1-x}Cd_xS$ interface mediated heterostructure, this CdS sensitized $Zn_{1-x}Cd_xS$@ZnS core@shell heterostructure can take full advantage of excellent stability of ZnS, high photocatalytic activity of CdS, and tunable parameters of $Zn_{1-x}Cd_xS$. Moreover, the porous ZnS shell could dramatically improve the transport of reactants.[17,28]

4. CONCLUSION

In summary, various novel ternary heterostructures were fabricated using ZnS, CdS, and $Zn_{1-x}Cd_xS$ with different features as the composed semiconductors. Both the morphology and semiconductor configuration were facilely modulated via a one-pot hydrothermal method using the different solvents with different molecular structures as precursors. The photocatalytic activity was found to depend on the morphology, especially the semiconductor configuration, and the rational designed CdS sensitized porous $Zn_{1-x}Cd_xS$@ZnS core@shell heterostructure, which completely utilize the features of these semiconductors, showing the optimal photocatalytic activity of 100.2 mmol/h/g and best photocatalytic stability. This excellent H_2-production rate is 143- and 911-times higher than those of CdS prepared using DETA and DIW as solvents, respectively, and it is also considerably better than other CdS-based heterostructures.

■ ASSOCIATED CONTENT

Supporting Information

The Supporting Information is available free of charge on the ACS Publications website at DOI: 10.1021/acsami.5b11388.

DOI: 10.1021/acsami.5b11388
ACS Appl. Mater. Interfaces 2016, 8, 4516−4522

Additional XRD, UV−vis, SEM, TEM, EDX, ICP, and XPS results; absorption/desorption isotherms; Nyquist plots; PL spectra (PDF)

AUTHOR INFORMATION

Corresponding Authors

*E-mail: yqlan@njnu.edu.cn.
*E-mail: baojianchun@njnu.edu.cn.

Notes

The authors declare no competing financial interest.

ACKNOWLEDGMENTS

This work was financially supported by NSFC (No. 21371099 and 21471080), the Jiangsu Specially-Appointed Professor, the NSF of Jiangsu Province of China (No. BK20130043 and BK20141445), the Natural Science Research of Jiangsu Higher Education Institutions of China (No. 13KJB150021), the Priority Academic Program Development of Jiangsu Higher Education Institutions, and the Foundation of Jiangsu Collaborative Innovation Center of Biomedical Functional Materials.

REFERENCES

(1) Chen, X.; Shen, S.; Guo, L.; Mao, S. S. Semiconductor-based Photocatalytic Hydrogen Generation. *Chem. Rev.* **2010**, *110*, 6503−6570.

(2) Wang, H.; Zhang, L.; Chen, Z.; Hu, J.; Li, S.; Wang, Z.; Liu, J.; Wang, X. Semiconductor Heterojunction Photocatalysts: Design, Construction, and Photocatalytic Performances. *Chem. Soc. Rev.* **2014**, *43*, 5234−5244.

(3) Yu, Y.; Zhang, J.; Wu, X.; Zhao, W.; Zhang, B. Nanoporous Single-Crystal-Like $Cd_xZn_{1-x}S$ Nanosheets Fabricated by the Cation-Exchange Reaction of Inorganic−Organic Hybrid ZnS−Amine with Cadmium Ions. *Angew. Chem., Int. Ed.* **2012**, *51*, 897−900.

(4) Pan, C. S.; Xu, J.; Wang, Y. J.; Li, D.; Zhu, Y. F. Dramatic Activity of $C_3N_4/BiPO_4$ Photocatalyst with Core/Shell Structure Formed by Self-Assembly. *Adv. Funct. Mater.* **2012**, *22*, 1518−1524.

(5) Zhukovskyi, M.; Tongying, P.; Yashan, H.; Wang, Y.; Kuno, M. Efficient Photocatalytic Hydrogen Generation from Ni Nanoparticle Decorated CdS Nanosheets. *ACS Catal.* **2015**, *5*, 6615−6623.

(6) Tian, J.; Leng, Y. H.; Zhao, Z. H.; Xia, Y.; Sang, Y. H.; Hao, P.; Zhan, J.; Li, M. C.; Liu, H. Carbon Quantum Dots/hydrogenated TiO_2 Nanobelt Heterostructures and Their Broad Spectrum Photocatalytic Properties under UV, Visible, and Near-infrared Irradiation. *Nano Energy* **2015**, *11*, 419−427.

(7) Yu, J.; Xu, C.-Y.; Ma, F.-X.; Hu, S.-P.; Zhang, Y.-W.; Zhen, L. Monodisperse SnS_2 Nanosheets for High-Performance Photocatalytic Hydrogen Generation. *ACS Appl. Mater. Interfaces* **2014**, *6*, 22370−22377.

(8) Huang, L.; Wang, X.; Yang, J.; Liu, G.; Han, J.; Li, C. Dual Cocatalysts Loaded Type I CdS/ZnS Core/Shell Nanocrystals as Effective and Stable Photocatalysts for H_2 Evolution. *J. Phys. Chem. C* **2013**, *117*, 11584−11591.

(9) Zhang, J.; Yu, J.; Zhang, Y.; Li, Q.; Gong, J. R. Visible Light Photocatalytic H_2-Production Activity of CuS/ZnS Porous Nanosheets Based on Photoinduced Interfacial Charge Transfer. *Nano Lett.* **2011**, *11*, 4774−4779.

(10) Zhou, P.; Yu, J.; Jaroniec, M. All-Solid-State Z-Scheme Photocatalytic Systems. *Adv. Mater.* **2014**, *26*, 4920−4935.

(11) McDaniel, H.; Pelton, M.; Oh, N.; Shim, M. Effects of Lattice Strain and Band Offset on Electron Transfer Rates in Type-II Nanorod Heterostructures. *J. Phys. Chem. Lett.* **2012**, *3*, 1094−1098.

(12) Zhang, N.; Yang, M.-Q.; Tang, Z.-R.; Xu, Y.-J. Toward Improving the Graphene−Semiconductor Composite Photoactivity via the Addition of Metal Ions as Generic Interfacial Mediator. *ACS Nano* **2014**, *8*, 623−633.

(13) Han, C.; Yang, M.-Q.; Zhang, N.; Xu, Y.-J. Enhancing the Visible Light Photocatalytic Performance of Ternary CdS-(graphene-Pd) Nanocomposites via a Facile Interfacial Mediator and Co-catalyst Strategy. *J. Mater. Chem. A* **2014**, *2*, 19156−19166.

(14) Yang, J.; Wang, D.; Han, H.; Li, C. Roles of Cocatalysts in Photocatalysis and Photoelectrocatalysis. *Acc. Chem. Res.* **2013**, *46*, 1900−1909.

(15) Wu, W.; Jiang, C.; Roy, V. A. L. Recent Progress in Magnetic Iron Oxide-Semiconductor Composite Nanomaterials as Promising Photocatalysts. *Nanoscale* **2014**, *7*, 38−58.

(16) Sun, L.; Wu, W.; Yang, S.; Zhou, J.; Hong, M.; Xiao, X.; Ren, F.; Jiang, C. Template and Silica Interlayer Tailorable Synthesis of Spindle-like Multilayer α-Fe_2O_3/Ag/SnO_2 Ternary Hybrid Architectures and Their Enhanced Photocatalytic Activity. *ACS Appl. Mater. Interfaces* **2014**, *6*, 1113−1124.

(17) Xie, Y. P.; Yu, Z. B.; Liu, G.; Ma, X. L.; Cheng, H.-M. CdS-mesoporous ZnS Core-shell Particles for Efficient and Stable Photocatalytic Hydrogen Evolution under Visible Light. *Energy Environ. Sci.* **2014**, *7*, 1895−1901.

(18) Kibsgaard, J.; Chen, Z.; Reinecke, B. N.; Jaramillo, T. F. Engineering the Surface Structure of MoS_2 to Preferentially Expose Active Edge Sites for Electrocatalysis. *Nat. Mater.* **2012**, *11*, 963−969.

(19) Shi, Y.; Guo, B.; Corr, S. A.; Shi, Q.; Hu, Y.-S.; Heier, K. R.; Chen, L.; Seshadri, R.; Stucky, G. D. Ordered Mesoporous Metallic MoO_2 Materials with Highly Reversible Lithium Storage Capacity. *Nano Lett.* **2009**, *9*, 4215−4220.

(20) Xie, J.; Zhang, H.; Li, S.; Wang, R.; Sun, X.; Zhou, M.; Zhou, J.; Lou, X. W.; Xie, Y. Defect-Rich MoS_2 Ultrathin Nanosheets with Additional Active Edge Sites for Enhanced Electrocatalytic Hydrogen Evolution. *Adv. Mater.* **2013**, *25*, 5807−5813.

(21) Wu, X.; Yu, Y.; Liu, Y.; Xu, Y.; Liu, C.; Zhang, B. Synthesis of Hollow $Cd_xZn_{1-x}Se$ Nanoframes through the Selective Cation Exchange of Inorganic−Organic Hybrid ZnSe−Amine Nanoflakes with Cadmium Ions. *Angew. Chem., Int. Ed.* **2012**, *51*, 3211−3215.

(22) Joo, J. B.; Lee, I.; Dahl, M.; Moon, G. D.; Zaera, F.; Yin, Y. D. Controllable Synthesis of Mesoporous TiO_2 Hollow Shells: Toward an Efficient Photocatalyst. *Adv. Funct. Mater.* **2013**, *23*, 4246−4254.

(23) Liu, S.; Zhang, N.; Tang, Z.-R.; Xu, Y.-J. Synthesis of One-Dimensional CdS@TiO_2 Core−Shell Nanocomposites Photocatalyst for Selective Redox: The Dual Role of TiO_2 Shell. *ACS Appl. Mater. Interfaces* **2012**, *4*, 6378−6385.

(24) Gao, M.; Zhu, L.; Ong, W. L.; Wang, J.; Ho, G. W. Structural Design of TiO_2-based Photocatalyst for H_2 Production and Degradation Applications. *Catal. Sci. Technol.* **2015**, *5*, 4703−4726.

(25) Zong, X.; Yan, H.; Wu, G.; Ma, G.; Wen, F.; Wang, L.; Li, C. Enhancement of Photocatalytic H_2 Evolution on CdS by Loading MoS_2 as Cocatalyst under Visible Light Irradiation. *J. Am. Chem. Soc.* **2008**, *130*, 7176−7177.

(26) Li, Q.; Guo, B.; Yu, J.; Ran, J.; Zhang, B.; Yan, H.; Gong, J. R. Highly Efficient Visible-Light-Driven Photocatalytic Hydrogen Production of CdS-Cluster-Decorated Graphene Nanosheets. *J. Am. Chem. Soc.* **2011**, *133*, 10878−10884.

(27) Li, S.; Chen, J.; Zheng, F.; Li, Y.; Huang, F. Synthesis of the Double-shell Anatase-rutile TiO_2 Hollow Spheres with Enhanced Photocatalytic Activity. *Nanoscale* **2013**, *5*, 12150−12155.

(28) Gao, P.; Liu, J.; Lee, S.; Zhang, T.; Sun, D. D. High Quality Graphene Oxide-CdS-Pt Nanocomposites for Efficient Photocatalytic Hydrogen Evolution. *J. Mater. Chem.* **2012**, *22*, 2292−2298.

(29) Li, Q.; Meng, H.; Zhou, P.; Zheng, Y.; Wang, J.; Yu, J.; Gong, J. $Zn_{1-x}Cd_xS$ Solid Solutions with Controlled Bandgap and Enhanced Visible-Light Photocatalytic H_2-Production Activity. *ACS Catal.* **2013**, *3*, 882−889.

(30) Li, K.; Chen, R.; Li, S.-L.; Han, M.; Xie, S.-L.; Bao, J.; Dai, Z.; Lan, Y.-Q. Self-assembly of a Mesoporous ZnS/mediating Interface/CdS Heterostructure with Enhanced Visible-light Hydrogen-production Activity and Excellent Stability. *Chem. Sci.* **2015**, *6*, 5263−5268.

(31) Zhang, J.; Wang, L.; Liu, X.; Li, X. a.; Huang, W. High-performance CdS-ZnS Core-shell Nanorod Array Photoelectrode for

DOI: 10.1021/acsami.5b11388
ACS Appl. Mater. Interfaces 2016, 8, 4516−4522

Photoelectrochemical Hydrogen Generation. *J. Mater. Chem. A* **2015**, *3*, 535−541.
(32) Shen, H. B.; Bai, X. W.; Wang, A.; Wang, H. Z.; Qian, L.; Yang, Y. X.; Titov, A.; Hyvonen, J.; Zheng, Y.; Li, L. S. High-Efficient Deep-Blue Light-Emitting Diodes by Using High Quality $Zn_xCd_{1-x}S$/ZnS Core/Shell Quantum Dots. *Adv. Funct. Mater.* **2014**, *24*, 2367−2373.
(33) Zhuang, T. T.; Yu, P.; Fan, F. J.; Wu, L.; Liu, X. J.; Yu, S. H. Controlled Synthesis of Kinked Ultrathin ZnS Nanorods/Nanowires Triggered by Chloride Ions: A Case Study. *Small* **2014**, *10*, 1394−1402.
(34) Zhang, J.; Wang, Y.; Jin, J.; Zhang, J.; Lin, Z.; Huang, F.; Yu, J. Efficient Visible-Light Photocatalytic Hydrogen Evolution and Enhanced Photostability of Core/Shell CdS/g-C_3N_4 Nanowires. *ACS Appl. Mater. Interfaces* **2013**, *5*, 10317−10324.
(35) Beberwyck, B. J.; Surendranath, Y.; Alivisatos, A. P. Cation Exchange: A Versatile Tool for Nanomaterials Synthesis. *J. Phys. Chem. C* **2013**, *117*, 19759−19770.
(36) Okun, N. M.; Ritorto, M. D.; Anderson, T. M.; Apkarian, R. P.; Hill, C. L. Polyoxometalates on Cationic Silica Nanoparticles. Physicochemical Properties of an Electrostatically Bound Multi-Iron Catalyst. *Chem. Mater.* **2004**, *16*, 2551−2558.
(37) Yu, J.; Zhang, J.; Jaroniec, M. Preparation and Enhanced Visible-light Photocatalytic H_2-production Activity of CdS Quantum Dots-sensitized $Zn_{1-x}Cd_xS$ Solid Solution. *Green Chem.* **2010**, *12*, 1611−1614.
(38) Zhu, J.; Yin, Z.; Yang, D.; Sun, T.; Yu, H.; Hoster, H. E.; Hng, H. H.; Zhang, H.; Yan, Q. Hierarchical Hollow Spheres Composed of Ultrathin Fe_2O_3 Nanosheets for Lithium Storage and Photocatalytic Water Oxidation. *Energy Environ. Sci.* **2013**, *6*, 987−993.
(39) Lim, J.; Jeong, B. G.; Park, M.; Kim, J. K.; Pietryga, J. M.; Park, Y.-S.; Klimov, V. I.; Lee, C.; Lee, D. C.; Bae, W. K. Influence of Shell Thickness on the Performance of Light-Emitting Devices Based on CdSe/$Zn_{1-X}Cd_XS$ Core/Shell Heterostructured Quantum Dots. *Adv. Mater.* **2014**, *26*, 8034−8040.
(40) Zhang, J.; Yu, J.; Jaroniec, M.; Gong, J. R. Noble Metal-Free Reduced Graphene Oxide-$Zn_xCd_{1-x}S$ Nanocomposite with Enhanced Solar Photocatalytic H_2-Production Performance. *Nano Lett.* **2012**, *12*, 4584−4589.
(41) Li, M.; Luo, W.; Cao, D.; Zhao, X.; Li, Z.; Yu, T.; Zou, Z. A Co-catalyst-Loaded Ta_3N_5 Photoanode with a High Solar Photocurrent for Water Splitting upon Facile Removal of the Surface Layer. *Angew. Chem., Int. Ed.* **2013**, *52*, 11016−11020.
(42) Wang, Q.; Li, J.; Bai, Y.; Lian, J.; Huang, H.; Li, Z.; Lei, Z.; Shangguan, W. Photochemical Preparation of Cd/CdS Photocatalysts and Their Efficient Photocatalytic Hydrogen Production under Visible Light Irradiation. *Green Chem.* **2014**, *16*, 2728−2735.
(43) Liu, J.; Liu, Y.; Liu, N.; Han, Y.; Zhang, X.; Huang, H.; Lifshitz, Y.; Lee, S.-T.; Zhong, J.; Kang, Z. Metal-free Efficient Photocatalyst for Stable Visible Water Splitting via a Two-electron Pathway. *Science* **2015**, *347*, 970−974.
(44) Becker, W. G.; Bard, A. J. Photoluminescence and Photoinduced Oxygen Adsorption of Colloidal Zinc Sulfide Dispersions. *J. Phys. Chem.* **1983**, *87*, 4888−4893.
(45) Rath, M. C.; Ramakrishna, G.; Mukherjee, T.; Ghosh, H. N. Electron Injection into the Surface States of ZrO_2 Nanoparticles from Photoexcited Quinizarin and Its Derivatives: Effect of Surface Modification. *J. Phys. Chem. B* **2005**, *109*, 20485−20492.
(46) Chawla, A. K.; Singhal, S.; Nagar, S.; Gupta, H. O.; Chandra, R. Study of Composition Dependent Structural, Optical, and Magnetic Properties of Cu-doped $Zn_{1-x}Cd_xS$ Nanoparticles. *J. Appl. Phys.* **2010**, *108*, 123519.
(47) Jayanthi, K.; Chawla, S.; Chander, H.; Haranath, D. Structural, Optical and Photoluminescence Properties of ZnS: Cu Nanoparticle Thin Films as a Function of Dopant Concentration and Quantum Confinement Effect. *Cryst. Res. Technol.* **2007**, *42*, 976−982.
(48) Yang, J.; Wang, B.; Cao, J.; Han, D.; Feng, B.; Wei, M.; Fan, L.; Kou, C.; Liu, Q.; Wang, T. Controllable Photoluminescent−magnetic Dual-encoded Wurtzite ZnS:$Cu^{2+}Mn^{2+}$ Nanowires Modulated by Cu^{2+} and Mn^{2+} Ions. *J. Alloys Compd.* **2013**, *574*, 240−245.
(49) Li, C. J.; Zhang, P.; Lv, R.; Lu, J. W.; Wang, T.; Wang, S. P.; Wang, H. F.; Gong, J. L. Selective Deposition of Ag_3PO_4 on Monoclinic $BiVO_4$(040) for Highly Efficient Photocatalysis. *Small* **2013**, *9*, 3951−3956.

DOI: 10.1021/acsami.5b11388
ACS Appl. Mater. Interfaces 2016, 8, 4516−4522